Suplemento de la Revista Mexicana de Física 3 040908 (2022) 1–10

PHENIX Spin Physics Overview

Dillon S. Fitzgerald[1†⋆]
1 *University of Michigan, Ann Arbor, MI, USA*
† *On behalf of the PHENIX collaboration*
⋆ *dillfitz@umich.edu*

Received 3 July 2022; accepted 15 September 2022

Understanding the spin structure of the proton is of large interest to the nuclear physics community and it is one of the main goals of the spin physics program at the Relativistic Heavy Ion Collider (RHIC). Measurements from data taken by the PHENIX detector with transverse ($p^{\uparrow}+p$, $p^{\uparrow}+Al$, $p^{\uparrow}+Au$) and longitudinal ($\vec{p}+\vec{p}$) proton polarization play an important role in this, in particular due to the leading order access to gluons in polarized protons. This is a crucially important counterpart to measurements made in lepton-hadron scattering experiments where gluons are not accessible at leading order. Transverse spin asymmetries provide insight into initial and final-state spin-momentum and spin-spin parton-hadron correlations, while longitudinal spin asymmetries provide access to parton polarization. A number of important recent PHENIX results and ongoing analyses will be presented, along with a discussion of how these measurements contribute to our understanding of proton spin structure.

Keywords: ***PHENIX, spin physics, spin asymmetries, longitudinal double-spin asymmetries, transverse single-spin asymmetries, direct photons, heavy flavor, charged pions, neutral mesons, jets, neutrons, gluon helicity, trigluon correlators***

1 Introduction

In the past few decades, we have vastly improved our understanding of proton structure from a naive picture where valence quarks carry all of the proton spin, to a much more complex picture involving spin and orbital angular momentum of constituent quarks and gluons. Collisions involving longitudinally polarized protons provide sensitivity to partonic spin contributions to the proton spin, while collisions involving transversely polarized protons allow for access to correlations between spin and orbital motion of partons with the proton spin. Figure 1 shows a table of transverse momentum dependent parton distribution functions (TMD PDFs), where the column and row headings represent nucleon and quark polarization respectively, and the diagonal elements highlighted in yellow survive integration over the partonic transverse momentum (k_T), including the familiar unpolarized PDFs, and the helicity distributions that provide access to partonic spin contributions.

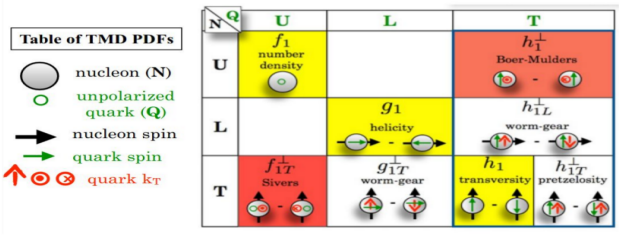

FIGURE 1. Table of TMD PDFs sorted by quark and nucleon polarization with k_T integrated distributions highlighted in yellow

1.1 Longitudinal Spin

The origin of the total proton spin $s = 1/2$ in terms of partonic contributions is of great interest and still under much investigation — it has been dubbed "the proton spin puzzle". Equation 1 shows the proton spin decomposed in terms of contributions from spin and angular momentum of quarks and gluons.

$$\frac{1}{2} = \frac{1}{2}\sum_q \Delta q + \Delta g + L_q + L_g \tag{1}$$

$\Delta q, g$ represents the quark and gluon helicity respectively, while $L_{q,g}$ represents the orbital angular momentum of quarks and gluons respectively. Δq is well constrained from lepton-hadron scattering experiments [1–3], while data from RHIC, the world's first and only polarized proton collider, allows for leading order access to gluons within polarized protons and significantly improved constraints on Δg. Figure 2 shows a fit including $\sqrt{s} = 200$ GeV $\vec{p}+\vec{p}$ data from RHIC taken in 2009 with significant improvements to the constraints on Δg, with evidence that it is positive for $x > 0.05$ [4]. Many measurements with a much larger dataset at $\sqrt{s} = 510$ GeV $\vec{p}+\vec{p}$ have since been published, allowing for an even more precise determination of Δg, and bringing us one step closer to solving the proton spin puzzle.

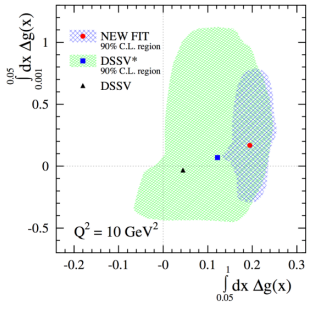

FIGURE 2. Moments of Δg in various regions of x, with the DSSV fit results, DSSV* fit results with the 90% confidence level (CL) region indicated by the green shaded area, and new fit results from [4] with the 90% CL region indicated by the blue shaded area

Longitudinal double-spin asymmetry measurements allow for access to parton helicity functions, and their contributions to the proton spin. They are defined as in Equation 2,

$$A_{LL} = \frac{\sigma^{++} - \sigma^{+-}}{\sigma^{++} + \sigma^{+-}} = \frac{\Delta\sigma}{\sigma}, \tag{2}$$

with $\sigma^{++,+-}$ representing the helicity-dependent cross-section of a particular reaction with $++$ denoting protons colliding the same (positive) helicity, and $+-$ denoting the case where the protons have opposite helicity. The helicity-dependent cross-section difference in the numerator of Equation 2 can be expressed as shown in Equation 3.

$$\Delta\sigma \propto \sum_{a,b} \Delta f_{a/A}(x_a) \otimes \Delta f_{b/B}(x_b) \otimes \Delta\sigma_{ab} \tag{3}$$

Here $\Delta f_{a/A}$ and $\Delta f_{b/B}$ are helicity distributions for partons within protons, and σ_{ab} is the partonic cross-section. Equations 2 and 3 show that longitudinal double-spin asymmetries provide direct access to parton helicity distributions.

1.2 Transverse Spin

The rich structure of protons gives rise to a number of spin-momentum and spin-spin correlations between the proton spin and the spin and momentum of the constituent partons, analogous to those in atomic systems. These correlations manifest experimentally via azimuthal modulations of produced and measured particles, and are accessible through measurements called transverse single-spin asymmetries, defined in Equation 4.

$$A_N(\phi) = \frac{\sigma^{\uparrow}(\phi) - \sigma^{\downarrow}(\phi)}{\sigma^{\uparrow}(\phi) + \sigma^{\downarrow}(\phi)} = A_N \cos\phi \tag{4}$$

$\sigma^{\uparrow,\downarrow}(\phi)$ are ϕ dependent cross-sections for different spin orientations, and $\cos\phi = \sin(\phi_{pol} - \phi)$ for $\phi_{pol} = \pm\pi/2$, corresponding to $\uparrow$ and $\downarrow$ spin orientations. Calculations based on perturbative QCD (pQCD) in [5] predict negligible contributions to TSSAs (<1%). While recent calculations suggest the possibility of some pQCD contributions [6], the large TSSAs seen in Figure 3 for $\pi^{\pm}$ measured as a function of $x_F = 2p_Z/\sqrt{s}$ at various facilities [7–11] and collision energies must arise from the nonpeturbative parts of the calculation.

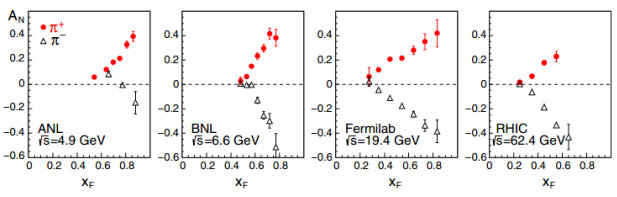

FIGURE 3. $A_N(x_F)$ for forward $\pi^{\pm}$ production measured at various collision energies of polarized proton-proton collisions [8–11]

Transverse single-spin asymmetry measurements have since gained a lot of attention as a means of characterizing the proton in terms of more than just the longitudinal momentum fraction of partons, and as a driving force in looking beyond leading twist to power-suppressed terms in the collinear factorization expansion (suppressed by $1/Q^{n-2}$ for twist-n). This has led to the development of two theoretical frameworks for describing observed TSSA measurements, one with explicit dependence on the transverse momentum k_T of partons within hadrons, where standard collinear parton distribution functions (PDFs) and fragmentation functions (FFs) are replaced with transverse-momentum-dependent (TMD) functions, and the other considering the effect of looking beyond leading twist (i.e. twist-2). To access TMD functions experimentally, both a soft scale k_T sensitive to partonic transverse momentum in the proton or process of hadronization and a hard-scattering energy scale Q are required, with $Q \gg k_T$, while the higher twist formalism requires only a hard scale Q. The TSSA measurements presented in this note are shown as a function of p_T of the produced particle, which we take as a proxy for Q. These measurements are therefore more relevant for constraining models within the higher twist formalism. However, unification of the two frameworks has been demonstrated, showing that twist-3 correlators are related to k_T moments of the corresponding TMD PDFs [12]. At twist-3, quantum interference between standard $2 \to 2$ QCD processes and those involving an extra gluon must be considered. This introduces additional terms to cross-section calculations that encode the interference in twist-3 correlation functions convoluted with standard collinear PDFs and FFs, with additional terms for every colliding or produced hadron. This is shown in Equation 5 for $A_N(p_A^{\uparrow} + p_B \to h_C + X)$ where h_C is particular final-state hadron.

$$\begin{aligned} A_N \propto & \sum_{a,b,c} \phi^{(3)}_{a/A}(x_1, x_2, \vec{s}_\perp) \otimes \phi_{b/B}(x') \otimes \hat{\sigma} \otimes D_{c\to C}(z) \\ & + \sum_{a,b,c} \delta q_{a/A}(x, \vec{s}_\perp) \otimes \phi^{(3)}_{b/B}(x'_1, x'_2) \otimes \hat{\sigma}' \otimes D_{c\to C}(z) \\ & + \sum_{a,b,c} \delta q_{a/A}(x, \vec{s}_\perp) \otimes \phi_{b/B}(x') \otimes \hat{\sigma}'' \otimes D^{(3)}_{c\to C}(z_1, z_2) \end{aligned} \tag{5}$$

Terms with a superscript (3) correspond to a twist-3 correlation functions, the rest are at leading twist (twist-2). The lower case subscripts represent the parton type while the uppercase subscripts represent the parent hadron. ϕ and D denote PDFs and FFs respectively, and $\delta q_{x/X}(x, \vec{s}_\perp)$ is the transversity distribution, a spin-spin correlation of transversely polarized quarks in transversely polarized hadrons [13]. The twist-3 correlators have more intuitive physical meaning through their relation to corresponding TMD PDFs [12, 14–16]. The choice of the final-state particle affects the sensitivity to different production channels and therefore the constraining power on twist-3 correlators of different parton types. In particular, the leading order access to gluons allows for constraints to be placed on trigluon correlation functions within polarized protons, related to the

gluon Sivers TMD. For example, heavy flavor production is dominated by gluon-gluon fusion at RHIC, and gluons do not have a transversity distribution in spin 1/2 nucleons, providing heightened sensitivity to the first term in Equation 5, and therefore the twist-3 trigluon correlation functions. Direct photons also provide clean access to constrain the trigluon correlation functions, as there are no fragmentation effects at leading order, and hence the third term in Equation 5 vanishes for this channel.

2 Apparatus

The Relativistic Heavy Ion Collider is the world's first polarized proton collider, allowing for spin physics measurements with leading order access to gluons at collider energies. The RHIC spin physics program complements existing lepton-hadron scattering experiments in its ability to constrain gluon helicity, twist-3 trigluon correlations, and gluon TMD PDFs. Figure 4 is a table of RHIC runs from 2006 to 2015 with the polarization fraction and the recorded luminosity displayed for both PHENIX and STAR for longitudinally and transversely polarized collisions. The blue box around the 2013 and 2015 runs indicates the datasets used for the majority of the measurements in this note — the 2013 run was the largest dataset of longitudinally polarized proton collisions at RHIC, with 155 pb^{-1} of recorded luminosity at PHENIX, and the 2015 run was the largest dataset of transversely polarized proton collisions at RHIC, with 60 pb^{-1} of recorded luminosity at PHENIX. In addition, the 2015 RHIC datasets for transversely polarized proton collisions with aluminum and gold are the only of their kind, allowing for some incredibly unique measurements, some of which are presented in this note.

Year	$\sqrt{s}$ (GeV)	Recorded Luminosity for longitudinally / transverse polarized p+p STAR	Recorded Luminosity for longitudinally / transverse polarized p+p PHENIX	<P> in %
2006	62.4	-- pb^{-1} / 0.2 pb^{-1}	0.08 pb^{-1} / 0.02 pb^{-1}	48
	200	6.8 pb^{-1} / 8.5 pb^{-1}	7.5 pb^{-1} / 2.7 pb^{-1}	57
2008	200	-- pb^{-1} / 7.8 pb^{-1}	-- pb^{-1} / 5.2 pb^{-1}	45
2009	200	25 pb^{-1} / -- pb^{-1}	16 pb^{-1} / -- pb^{-1}	55
	500	10 pb^{-1} / -- pb^{-1}	14 pb^{-1} / -- pb^{-1}	39
2011	500	12 pb^{-1} / 25 pb^{-1}	18 pb^{-1} / -- pb^{-1}	48
2012	200	-- pb^{-1} / 22 pb^{-1}	-- pb^{-1} / 9.7 pb^{-1}	61/56
	510	82 pb^{-1} / -- pb^{-1}	32 pb^{-1} / -- pb^{-1}	50/53
2013	510	300 pb^{-1} / -- pb^{-1}	155 pb^{-1} / -- pb^{-1}	51/52
2015	200	52 pb^{-1} / 52 pb^{-1}	-- pb^{-1} / 60 pb^{-1}	53/57
2015	200 p Au	total delivered Luminosity = 1.27 pb^{-1}		60
2015	200 p Al	total delivered Luminosity = 3.97 pb^{-1}		54

= Transversely polarized

FIGURE 4. Table of RHIC runs sorted by running year, collision energy, recorded luminosity for longitudinally and transversely polarized runs for PHENIX and STAR, and polarization fraction. The blue outline indicates the largest polarized p+p datasets from RHIC, measurements from which are presented in this note

Figure 5 shows the PHENIX detector as configured in 2012-2016, with the central arm spectrometers shown in the top panel, and the forward/backward detectors in the bottom panel. The central arm spectrometer has an acceptance of $|\eta| < 0.35$ and $\Delta\phi = 0.5$ per arm, and is comprised of drift and pad chambers for tracking and momentum measurements, a Ring-Imaging Cherenkov (RICH) detector for particle identification with e/π separation up to 4.9 GeV/c, electromagnetic calorimeters for measuring energy deposits with triggers used to select $e^{\pm}, \pi^{\pm}$, and γ, and hit patterns measured by layers of the silicon vertex detector (VTX) which are useful for removing conversion electrons. All of this provides detection capabilities for several particles including $\pi^{\pm}, e^{\pm}, \gamma, \pi^0, \eta$, and jets. The forward detectors are comprised of the muon arms, forward VTX detectors (FVTX), muon piston calorimeters (MPC), and the far forward zero degree calorimeters (ZDC). The forward detection system is capable of measuring particles including $\mu^{\pm}, n, \pi^0, \eta$. Finally, the beam beam counter is an event characterization detector used to measure the integrated luminosity, and the RHIC polarimeters are used to measure the beam polarization fraction. More information about the PHENIX detector can be found in the following reference [17].

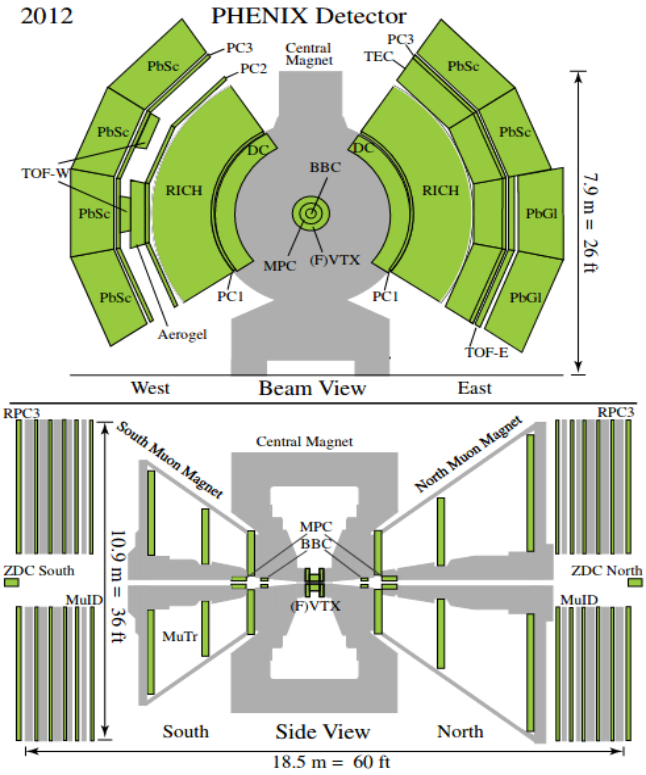

FIGURE 5. The PHENIX detector configuration in 2012 (relevant for the 2013 and 2015 data taking), showing the central arm spectrometers in the top panel and the forward/backward detectors in the bottom panel

3 Results

The results shown include A_{LL} measurements for midrapidity $\pi^{\pm}$, direct γ, and jets at $\sqrt{s} = 510$ GeV, and A_N measurements for midrapidity π^0, η, heavy flavor decay $e^{\pm}$ and for-

ward $\mu^{\pm}, n$, and unidentified charged hadrons at $\sqrt{s} = 200$ GeV. Figures 6 and 7 show the partonic subprocess fractions from simulation for pions and jets [18] respectively, with the solid lines representing $\sqrt{s} = 200\,GeV$ and $\sqrt{s} = 510\,GeV$.

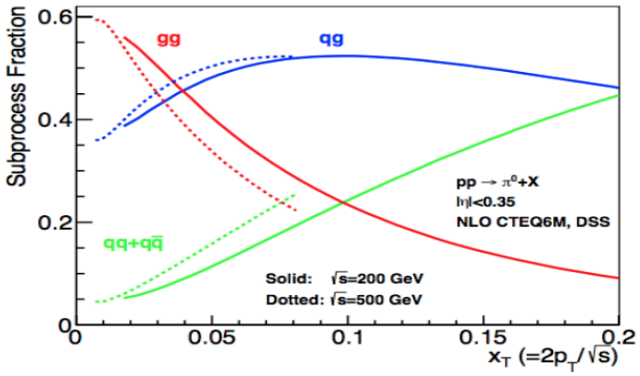

FIGURE 6. Partonic subprocesses fraction for midrapidity π^0 production, with the solid and dashed lines representing $\sqrt{s} = 200$ and $500\,GeV$ respectively

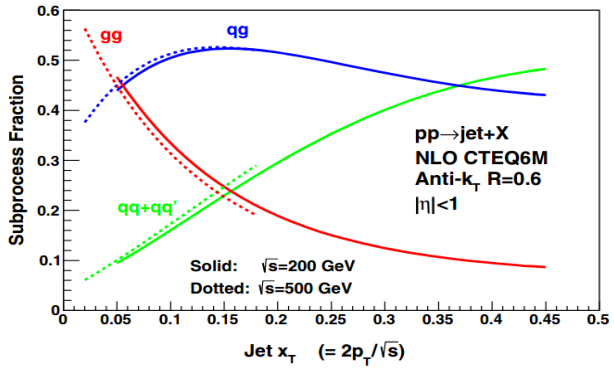

FIGURE 7. Partonic subprocesses fraction for anti-k_T jets with R=0.6 at midrapidity from Ref. [18], with the solid and dashed lines representing $\sqrt{s} = 200$ and $500\,GeV$ respectively

Both figures indicate that for these production channels, $2 \to 2$ processes involving gluons dominate below $20\,GeV$, with quark-gluon scattering dominating in the region $5 - 20$ GeV. In addition, direct photons are dominantly produced via the quark-gluon Compton scattering process, and heavy flavor hadrons are dominantly produced from gluon-gluon fusion.

3.1 Longitudinal Spin

Figures 8 and 9 are the longitudinal double-spin asymmetries for midrapidity charged pions with $\sqrt{s} = 510\,GeV$ plotted as a function of p_T and $x_T = 2p_T/\sqrt{s}$ respectively [19]. Figure 8 shows the π^+ plotted as blue squares, the π^- as red circles, and the π^0, measured in [20], as black circles. The DSSV fits from [4] are plotted alongside the data with with long, short, and medium length dashes for π^+, π^-, and π^0 respectively, and with the same color coding as the data points (blue, red, and black respectively). Figure 8 shows consistency amongst each respective pion type ($\pi^{\pm}, \pi^0$) and the corresponding DSSV14 fit. Figure 9 shows the double-spin asymmetry plotted as a function of x_T with a measured x_T range corresponding to $0.04 \lessapprox x_B \lessapprox 0.09$. Blue squares and red circles are used again for π^+ and π^- for this measurement, in addition to purple upward triangles for π^+ and black downward triangles for π^- for a previous PHENIX measurement at $\sqrt{s} = 200\,GeV$ [21], where a significant increase of precision was achieved in a complementary region of x_T.

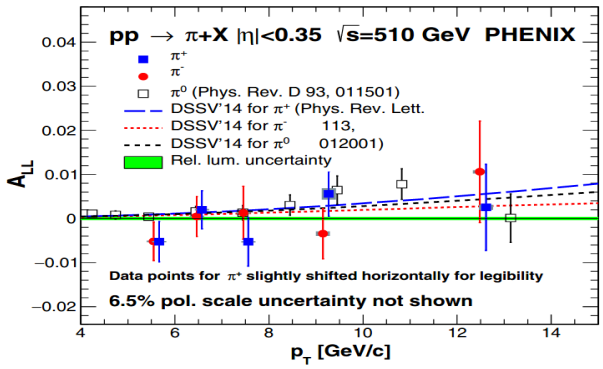

FIGURE 8. Longitudinal double-spin asymmetry measured as a function of p_T for midrapidity $\pi^{\pm}$ production at $\sqrt{s} = 510$ GeV [19] (blue squares/red circles) plotted alongside DSSV14 fits [4] and the π^0 results from [20] (black open squares)

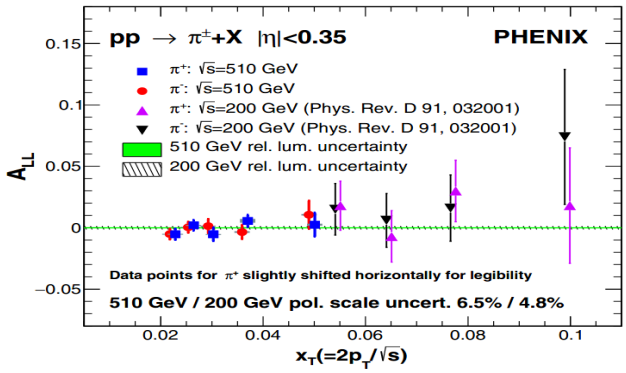

FIGURE 9. Longitudinal double-spin asymmetry measured as a function of x_T for midrapidity $\pi^{\pm}$ production at $\sqrt{s} = 510$ GeV [19] (blue squares/red circles) plotted alongside previous $\sqrt{s} = 200\,GeV$ $\pi^{\pm}$ results from Ref. [21] (upward purple triangles/downward black triangles)

Figure 10 shows A_{LL} for midrapidity jets as a function of p_T with $\sqrt{s} = 510\,GeV$ in black circles, reconstructed with a radius parameter of $R = 0.3$ using the anti-k_T algorithm, plotted alongside NLO + $\ln R$ theoretical predictions from Kang and Ringer taking into account DSSV14 fits, and a measurement of jet A_{LL} from STAR at $\sqrt{s} = 510\,GeV$ in red circles, reconstructed with a radius parameter of $R = 0.6$. This PHENIX preliminary measurement is consistent with both the measurement from STAR and the theoretical predic-

tions from Kang and Ringer. It should be noted that a rather small radius parameter of $R = 0.3$ is used due to the acceptance of the PHENIX central arm spectrometer $|\eta| < 0.35$, and that the bins are correlated from the unfolding procedure.

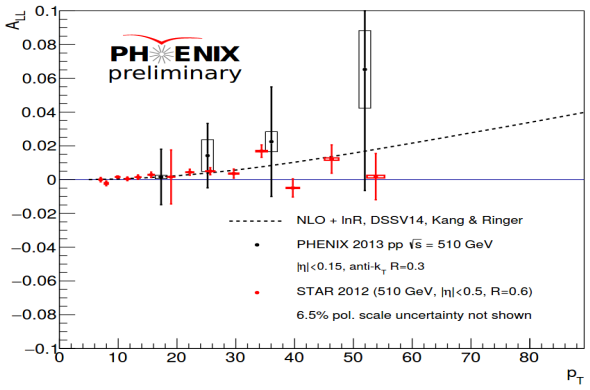

FIGURE 10. Longitudinal double-spin asymmetry as a function of p_T for midrapidity anti-k_T jets with $R = 0.3$ at $\sqrt{s} = 510\ GeV$ (black points) plotted alongside a midrapidity STAR anti-k_T jet A_{LL} measurement with $R = 0.6$ (red points) and theoretical predictions from Kang and Ringer

Figure 11 shows the midrapidity direct photon A_{LL} as a function of p_T measured at $\sqrt{s} = 510\ GeV$ [22]. This is the first longitudinal double-spin asymmetry measurement for direct photons to date. The dominant production mechanism for direct photons with $p_T > 5\ GeV/c$ is quark-gluon Compton scattering $qg \to q\gamma$, which is free from final-state fragmentation effects, allowing for direct access to helicity distributions in the colliding protons. To access direct photons experimentally, an isolation criteria is applied in a cone around the γ to remove background from hadronic decays. This observable is sensitive to both the sign and magnitude of Δg for direct photon production, and was therefore proposed to be a *golden channel* for accessing gluonic spin contributions in the 1992 RHIC-spin proposal [23, 24].

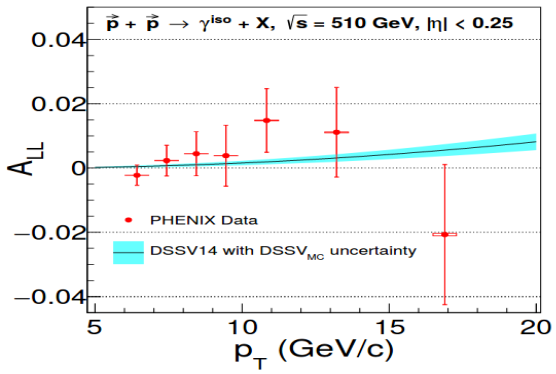

FIGURE 11. Longitudinal double-spin asymmetry measured as a function of p_T for midrapidity direct γ production at $\sqrt{s} = 510\ GeV$ [22], plotted alongside fits from DSSV14

Each of the measurements presented in this section will contribute significantly to future fits in determining Δg. Figure 2 showed significant improvement on the constraints of Δg from inclusion of the $\sqrt{s} = 200\ GeV$ 2009 RHIC data. The $\sqrt{s} = 510\ GeV$ 2013 RHIC data has roughly an order of magnitude more recorded luminosity. The charged pion A_{LL} was published in 2020, while the direct photon A_{LL} has been submitted to PRL, and the jet A_{LL} is a PHENIX preliminary result. All of these measurements can soon be included into future fits for extracting Δg with more stringent constraints than ever before.

3.2 Transverse Spin

Figure 12 shows the transverse single-spin asymmetry A_N as a function of p_T for midrapidity π^- in red circles and π^+ in blue triangles with $\sqrt{s} = 200\ GeV$ from Ref. [25], plotted alongside the TSSA for π^0 at $\sqrt{s} = 200\ GeV$ from Ref. [26], and theoretical predictions considering contributions from twist-3 quark gluon quark (qgq) correlation functions from Cammarota, et al. These are the first results of midrapidity charged pion A_N from PHENIX. They are consistent with zero and the π^0 results, but there is an indication that $\pi^\pm$ behave differently as a function of p_T, exhibiting a potential flavor, similarly to the theoretical calculations.

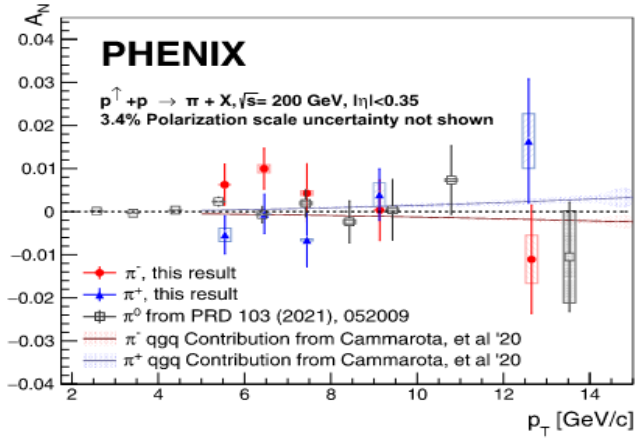

FIGURE 12. Transverse single-spin asymmetry as a function of p_T for midrapidity $\pi^\pm$ production at $\sqrt{s} = 200\ GeV$ (blue triangles/red circles) from Ref. [25], plotted alongside the π^0 results from Ref. [26] (black open squares), and theoretical predictions taking into account contributions from twist-3 qgq correlators from Cammarota et al

Figure 13 shows A_N as a function of p_T for midrapidity neutral pions in blue circles and midrapidity eta mesons in red squares with $\sqrt{s} = 200\ GeV$ from Ref. [26]. Both π^0 and η results have a higher reach in p_T, and a factor of 3 increase in statistical precision compared with previous PHENIX results [27], and both are consistent with zero. Figure 14 shows the π^0 A_N result again in blue circles plotted alongside theoretical predictions for twist-3 qgq correlator contributions, and from the Generalized Parton Model (GPM) [28]. This

result is useful in constraining the twist-3 trigluon correlation functions [29], as well as the gluon Sivers TMD function in the GPM [28], while the eta result in particular is sensitive to strangeness effects in twist-3 correlation functions.

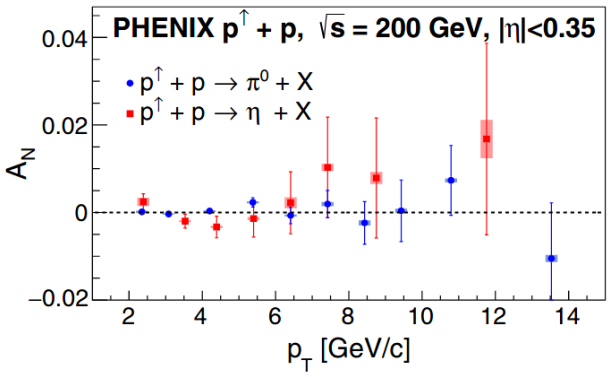

FIGURE 13. Transverse single-spin asymmetry as a function of p_T for midrapidity π^0 and η production at $\sqrt{s} = 200\ GeV$ from Ref. [26] plotted with blue circles and red squares respectively

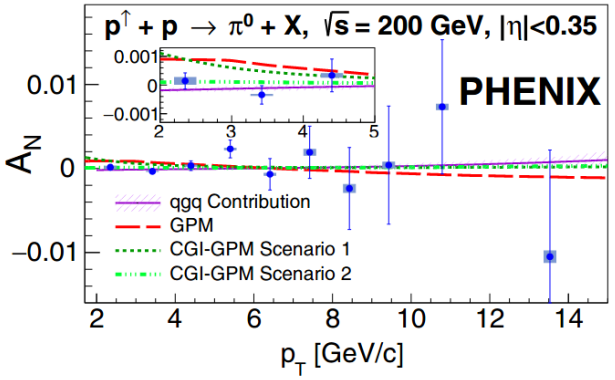

FIGURE 14. Transverse single-spin asymmetry for midrapidity π^0 production from Figure 13 plotted alongside several theoretical predictions, including those in the GPM from Ref. [28]

The midrapidity direct photon $A_N(p_T)$ with $\sqrt{s} = 200\ GeV$ from Ref. [30] is shown in Figure 15 in black circles, plotted alongside theoretical predictions for contributions from twist-3 qgq and trigluon ggg correlators. It is the first midrapidity direct photon TSSA measurement at RHIC, with a 50 fold improvement in precision with respect to the only previous measurement for this observable carried out by the Fermilab E704 experiment [31]. The measurement is consistent with zero in the measured p_T range within $\approx 2\%$. As mentioned before, direct photon production is an excellent channel for accessing gluons in the initial state, due to the lack of final-state fragmentation effects and quark-gluon Compton scattering being the dominant production mechanism. Direct γ A_N is therefore an excellent observable for constraining the trigluon correlation functions [32].

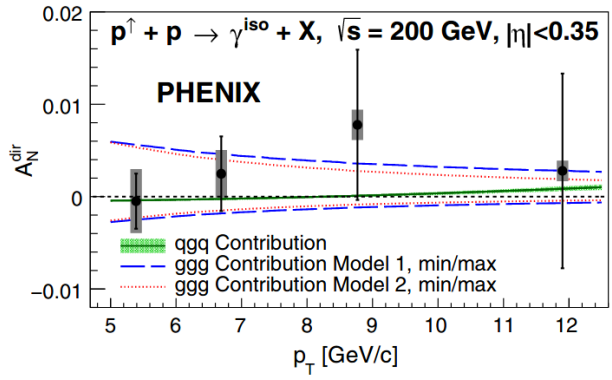

FIGURE 15. Transverse single-spin asymmetry as a function of p_T for direct γ production at $\sqrt{s} = 200\ GeV$ [30], plotted alongside several theoretical predictions considering contributions from qgq correlators, and from trigluon correlators [32]

Figure 16 shows the midrapidity open heavy flavor decay $e^{\pm}$ TSSA as a function of p_T with $\sqrt{s} = 200\ GeV$ from Ref. [33] (e^+ in red circles, e^- in blue squares), which has been submitted to PRL. The data is plotted alongside theoretical predictions from [34, 35] for model parameters that best fit the e^+ and e^- TSSA data simultaneously. The model parameters (λ_f, λ_d) correspond to normalization parameters of the antisymmetric and symmetric trigluon correlators to the unpolarized gluon PDF ($g(x)$) respectively [34], while similarly, K_G and K'_G correspond to normalization parameters of both trigluon correlators to the unpolarized gluon PDF from Ref. [35], each with separate functional dependence on x in the normalization to $g(x)$. In models with $A_N(\lambda_f, \lambda_d)$ and $A_N(K'_G)$, the model parameters that fit the data best yield predictions for A_N with opposite signs for the separate charges. The data for e^+ and e^- are consistent with zero, as well as with the theory curves with best-fit model parameters. The best-fit model parameters are determined by performing scans in parameter space, and calculating $A_N^{\lambda_f,\lambda_d}(p_T)$, $A_N^{K_G}(p_T)$, and $A_N^{K'_G}(p_T)$ for $D \to e^+$ and $\bar{D} \to e^-$ separately. The results are compared to data in each p_T bin for each parameter value, and $\chi^2(\lambda_f, \lambda_d) = \chi^2_{e^+}(\lambda_f, \lambda_d) + \chi^2_{e^-}(\lambda_f, \lambda_d)$, $\chi^2(K_G) = \chi^2_{e^+}(K_G) + \chi^2_{e^-}(K_G)$, and $\chi^2(K'_G) = \chi^2_{e^+}(K'_G) + \chi^2_{e^-}(K'_G)$ distributions are calculated, from which the minimum values are used to determine the best-fit model parameters. The results of the scan for (λ_f, λ_d) are shown in Figure 17, where $\Delta\chi^2_{e^\pm}(\lambda_f, \lambda_d) = \chi^2_{e^\pm}(\lambda_f, \lambda_d) - \chi^2_{e^\pm \min}$ distributions are shown for e^+ in panel (a) and e^- in panel (b), while panel (c) depicts the the values of (λ_f, λ_d) that correspond to χ^2_{min} for both charges combined as well as 1, 2, and 3 σ confidence level regions, calculated as $\Delta\chi^2 < n^2$ for $n = 1, 2$, and 3. This gives 1σ confidence intervals of ($\lambda_f = -0.01 \pm 0.03$ GeV, $\lambda_d = 0.11 \pm 0.11$ GeV). A similar procedure is performed for K_G and K'_G yielding $K_G = 0.0006^{+0.0014}_{-0.0017}$ and $K'_G = 0.00025 \pm 0.00025$. This represents the first set of experimental constraints for the normalization parameters of trigluon correlators to the unpolarized gluon PDF.

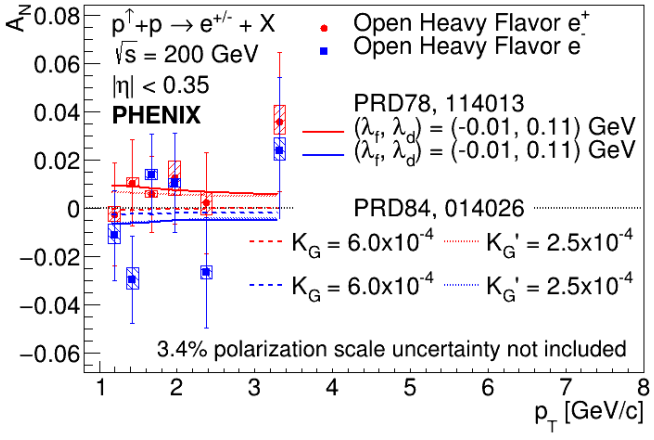

FIGURE 16. Transverse single-spin asymmetry as a function of p_T for midrapidity heavy flavor $e^{\pm}$ production at $\sqrt{s} = 200\ GeV$ [33] (red circles/blue squares) plotted alongside theoretical predictions of from Refs. [34, 35] for best-fit trigluon correlator normalization parameters (solid, dashed, and dotted red/blue lines)

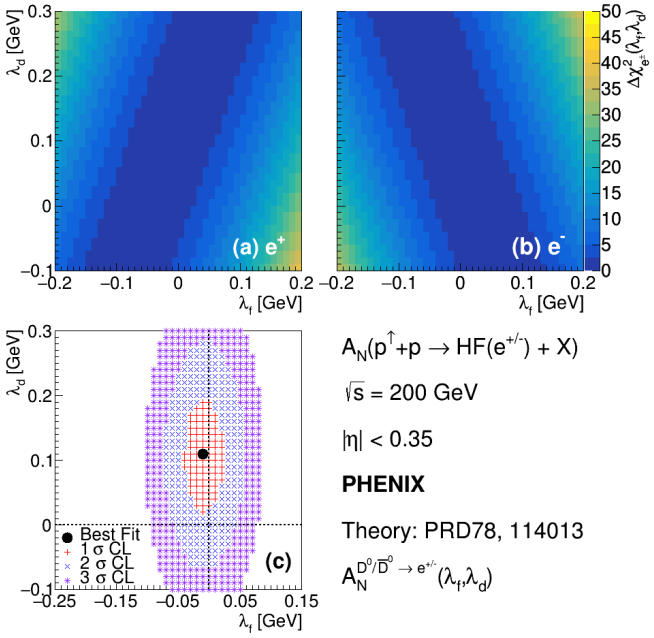

FIGURE 17. Results of the statistical analysis performed to extract best-fit model parameters λ_f and λ_d by comparing data to theory [34]. $\chi^2(\lambda_f, \lambda_d) - \chi^2_{\min}$ is shown for (a) e^+, and (b) e^-. (c): 1, 2, and 3σ confidence level regions, $\chi^2(\lambda_f, \lambda_d) - \chi^2_{min} < n^2$ $(n = 1, 2, 3)$

Figure 18 depicts the open heavy flavor decay muon A_N with $\sqrt{s} = 200\ GeV$ from Ref. [36] plotted as a function of p_T in the left panels and x_F in the right panels. The top panels show results for μ^- in blue and red circles, while the bottom show results for μ^+ in blue and red squares, and in each panel, the points with $x_F < 0$ (backward rapidity) are plotted in blue on the left while the points with $x_F > 0$ (forward rapidity) are plotted in red on the right. In each panel, the data is plotted alongside theoretical predictions from Ref. [35] with two phenomenological models (solid and dashed black curves) including contributions from trigluon correlation functions — these correspond to model parameters K_G and K'_G constrained by the new heavy flavor electron result [33]. This measurement was performed using the 2012 PHENIX dataset, and a follow up measurement is planned for the 2015 dataset with ≈ 6.5 times the integrated luminosity.

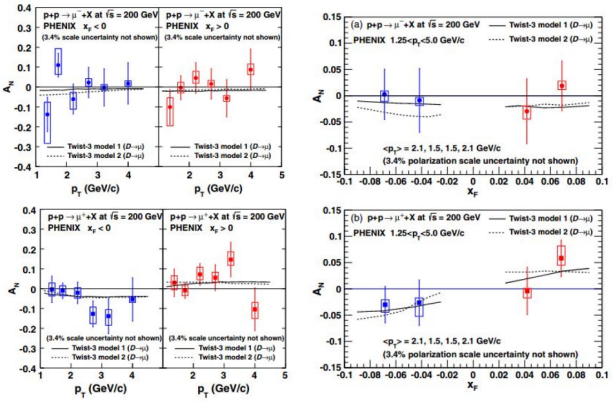

FIGURE 18. Transverse single-spin asymmetry as a function of p_T (left panels) and x_F (right panels) for forward μ^- (top panels) and μ^+ (bottom panels) production at $\sqrt{s} = 200\ GeV$ from Ref. [36], plotted alongside theoretical predictions considerting contributions from ggg correlators [35]

The forward positively charged hadron $A_N(\phi)$ measured at $\sqrt{s_{NN}} = 200\ GeV$ in $p^\uparrow + p$, $p^\uparrow + Al$, and $p^\uparrow + Au$ collisions from Ref. [37] is shown in Figure 19. This measurement includes $\pi^+/K^+/p$ with proportions of roughly $0.45/0.47/0.05$. A clear suppression of the amplitude A_N can be seen in collisions with heavier nuclei. This suppression can be seen again in Figure 20 with A_N plotted as a function of the cube root of mass-number A in the left panel and $N_{\text{coll}}^{\text{Avg}}$ in the right panel. While the data is consistent with an $A^{1/3}$ suppression predicted in models with gluon saturation effects [38, 39], it is important to note that the average p_T for this measurement is above the expected saturation scale for Au.

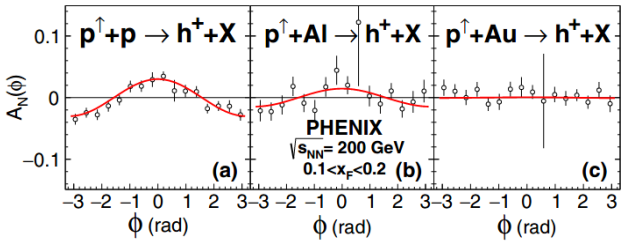

FIGURE 19. Transverse single-spin asymmetry measured as a function of ϕ for forward positively charged hadron production in $\sqrt{s_{NN}} = 200\ GeV$ $p^\uparrow + p, p^\uparrow + Al$, and $p^\uparrow + Au$ collisions [37]

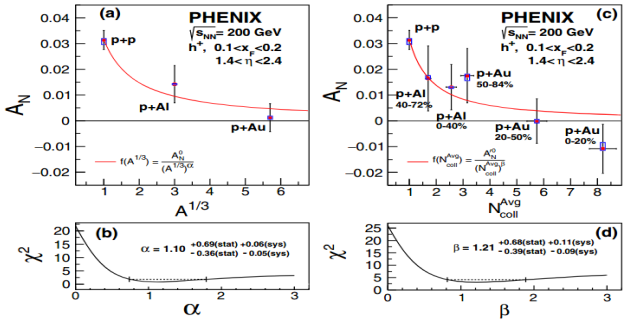

FIGURE 20. Transverse single-spin asymmetry measured as a function of the cube root of mass number A (left panel) and $N_{\rm coll}^{\rm Avg}$ for forward positively charged hadrons in $\sqrt{s_{NN}} = 200\ GeV$ $p^{\uparrow}+p, p^{\uparrow}+Al$, and $p^{\uparrow}+Au$ collisions [37]

Figures 21 and 22 depict very forward TSSA measurements as a function of p_T and x_F for neutrons in $p^{\uparrow}+p$, $p^{\uparrow}+Al$, and $p^{\uparrow}+Au$ collisions at $\sqrt{s_{NN}} = 200\ GeV$ from Ref. [40] for beam-beam-counter(BBC) tagged events dominated by hadronic interactions, and BBC vetoed events (with little activity in the BBC) that show an enhancement of ultra peripheral collisions (UPC) respectively. In both figures, the blue triangles are for $p^{\uparrow}+p$ collisions, the green squares are for $p^{\uparrow}+Al$ collisions, and the red circles for $p^{\uparrow}+Au$ collisions. Each panel is plotted as a function of p_T, while the individual panels represent different x_F bins. Theoretical predictions provided by Mitsuka [41,42] with contributions from UPC and one pion exchange (OPE) processes are plotted alongside the data for each collision system (with the same color coding). The asymmetries tend to be negative in the BBC tagged case for each collision system, but in the BBC vetoed case, the asymmetries tend to be positive and grow quite large due to the enhancement in UPC, which can be seen by the increase in magnitude of A_N for collisions with successively heavier nuclei. While the asymmetries agree qualitatively with the theory curves, there are still fairly large discrepancies in various regions of p_T and x_F.

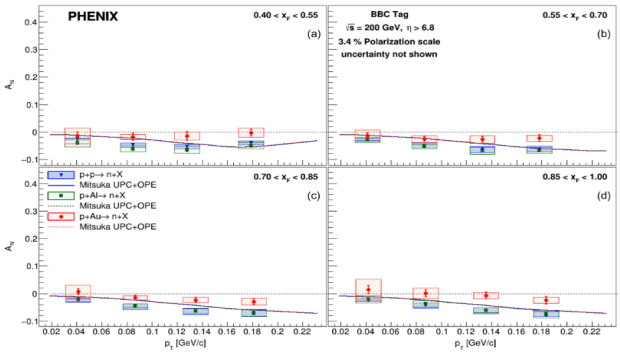

FIGURE 21. Transverse single-spin asymmetry measured as a function of p_T (horizontal axis) and x_F (4 panels) for forward neutron production in $\sqrt{s_{NN}} = 200\ GeV$ $p^{\uparrow}+p$ (blue triangles), $p^{\uparrow}+Al$ (green squares), and $p^{\uparrow}+Au$ (red circles) collisions [40] for BBC tagged events, with an enhancement in hadronic interactions, plotted along side theory predictions from Mitsuka with contributions from UPC and OPE interactions from Ref. [41] based on Ref. [42]

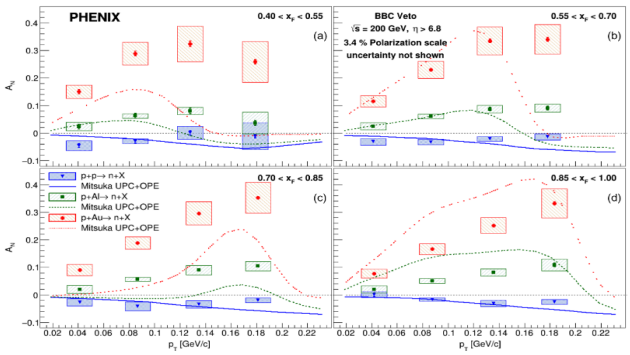

FIGURE 22. Transverse single-spin asymmetry measured as a function of p_T (horizontal axis) and x_F (4 panels) for forward neutron production in $\sqrt{s_{NN}} = 200\ GeV$ $p^{\uparrow}+p$ (blue triangles), $p^{\uparrow}+Al$ (green squares), and $p^{\uparrow}+Au$ (red circles) collisions [40] for BBC vetoed events, with an enhancement in UPC as the atomic number Z increases, plotted along side theory predictions from Mitsuka with contributions from UPC and OPE interactions from Ref. [41], based on Ref. [42]

All of the TSSA measurements at PHENIX presented in this note contribute significantly to our understanding of transverse spin physics and polarized proton structure. From multiple measurements with the ability to constrain the previously unconstrained trigluon correlation functions, to measurements on the incredibly unique $p^{\uparrow}+A$ datasets that continue to yield surprising results and new insights.

4 Conclusions

In conclusion, the PHENIX spin physics program continues to provide insight into many remaining mysteries in QCD, from the gluonic contributions to the proton spin, to developing a clearer picture of the theoretical origins of observed TSSAs. The polarized proton collision datasets at RHIC are a crucial complement to lepton-hadron scattering experiments due to the leading order access to gluons, as the gluonic polarized PDFs are not as well constrained as their quark counterparts. Inclusion of the measurements presented in this note in global fits will play a key role in constraining gluon helicity, and twist-3 trigluon correlation functions, significantly improving our understanding of gluon dyanmics in polarized protons. In addition, measurements from the incredibly unique polarized $p^{\uparrow}+A$ data provide an opportunity to pin down the underlying mechanisms behind TSSAs and how they are affected in the presence of cold nuclear matter.

1. M. G. Alekseev et al., Quark helicity distributions from longitudinal spin asymmetries in muon-proton and muon-deuteron scattering, Phys. Lett. B 693 (2010) 227, 10.1016/j.physletb.2010.08.034
2. A. Airapetian et al., Quark helicity distributions in the nucleon for up, down, and strange quarks from semi-inclusive deep-inelastic scattering, Phys. Rev. D 71 (2005) 012003, 10.1103/PhysRevD.71.012003
3. H. Avakian et al., Measurement of Single and Double Spin Asymmetries in Deep Inelastic Pion Electroproduction with a Longitudinally Polarized Target, Phys. Rev. Lett. 105 (2010) 262002, 10.1103/PhysRevLett.105.262002
4. D. de Florian, et al., Evidence for Polarization of Gluons in the Proton, Phys. Rev. Lett. 113 (2014) 012001, 10.1103/PhysRevLett.113.012001
5. G. L. Kane, J. Pumplin, and W. Repko, Transverse Quark Polarization in Large-p_T Reactions, e^+e^- Jets, and Leptoproduction: A Test of Quantum Chromodynamics, Phys. Rev. Lett. 41 (1978) 1689, 10.1103/PhysRevLett.41.1689
6. S. Benic, et al., Single-spin asymmetries at two loops, Phys. Rev. D 100 (2019) 094027, 10.1103/PhysRevD.100.094027
7. C. A. Aidala, et al., The spin structure of the nucleon, Rev. Mod. Phys. 85 (2013) 655, 10.1103/RevModPhys.85.655
8. R. D. Klem, et al., Measurement of Asymmetries of Inclusive Pion Production in Proton Proton Interactions at 6-GeV/c and 11.8-GeV/c, Phys. Rev. Lett. 36 (1976) 929, 10.1103/PhysRevLett.36.929
9. D. L. Adams et al., Analyzing power in inclusive π^+ and π^- production at high x_F with a 200-GeV polarized proton beam, Phys. Lett. 264 (1991) 462, 10.1016/0370-2693(91)90378-4
10. C. Allgower et al., Measurement of analyzing powers of π^+ and π^- produced on a hydrogen and a carbon target with a 22-GeV/c incident polarized proton beam, Phys. Rev. D 65 (2002) 092008, 10.1103/PhysRevD.65.092008
11. I. Arsene et al., Single Transverse Spin Asymmetries of Identified Charged Hadrons in Polarized $p+p$ Collisions at $\sqrt{s}$ = 62.4 GeV, Phys. Rev. Lett. 101 (2008) 042001, 10.1103/PhysRevLett.101.042001
12. X. Ji, et al., A Unified picture for single transverse-spin asymmetries in hard processes, Phys. Rev. Lett. 97 (2006) 082002, 10.1103/PhysRevLett.97.082002
13. J. P. Ralston and D. E. Soper, Production of dimuons from high-energy polarized proton-proton collisions, Nuclear Physics B 152 (1979) 109, https://doi.org/10.1016/0550-3213(79)90082-8
14. D. Sivers, Single-spin production asymmetries from the hard scattering of pointlike constituents, Phys. Rev. D 41 (1990) 83, 10.1103/PhysRevD.41.83
15. D. Boer and P. J. Mulders, Time-reversal odd distribution functions in leptoproduction, Phys. Rev. D 57 (1998) 5780, 10.1103/PhysRevD.57.5780
16. J. Collins, Fragmentation of transversely polarized quarks probed in transverse momentum distributions, Nuclear Physics B 396 (1993) 161, https://doi.org/10.1016/0550-3213(93)90262-N
17. K. Adcox et al., PHENIX detector overview, Nucl. Instrum. Meth. A 499 (2003) 469, 10.1016/S0168-9002(02)01950-2
18. J. Adam et al., Longitudinal double-spin asymmetry for inclusive jet and dijet production in pp collisions at $\sqrt{s} = 510$ GeV, Phys. Rev. D 100 (2019) 052005, 10.1103/PhysRevD.100.052005
19. U. A. Acharya et al., Measurement of charged pion double spin asymmetries at midrapidity in longitudinally polarized $p+p$ collisions at $\sqrt{s}$ = 510 GeV, Phys. Rev. D 102 (2020) 032001, 10.1103/PhysRevD.102.032001
20. A. Adare et al., Inclusive cross section and double-helicity asymmetry for π^0 production at midrapidity in $p+p$ collisions at $\sqrt{s} = 510$ GeV, Phys. Rev. D 93 (2016) 011501, 10.1103/PhysRevD.93.011501
21. A. Adare et al., Charged-pion cross sections and double-helicity asymmetries in polarized p+p collisions at $\sqrt{s}$=200 GeV, Phys. Rev. D 91 (2015) 032001, 10.1103/PhysRevD.91.032001
22. U. A. Acharya et al., Measurement of Direct-Photon Cross Section and Double-Helicity Asymmetry at $\sqrt{s} = 510$ GeV in $\vec{p}+\vec{p}$ Collisions (2022)
23. G. Bunce, et al., Proposal on spin physics using the RHIC polarized collider (1992), 10.2172/1151313
24. G. Bunce, et al., Prospects for spin physics at RHIC, Ann. Rev. Nucl. Part. Sci. 50 (2000) 525, 10.1146/annurev.nucl.50.1.525
25. U. A. Acharya et al., Transverse-single-spin asymmetries of charged pions at midrapidity in transversely polarized $p+p$ collisions at $\sqrt{s} = 200$ GeV, Phys. Rev. D 105 (2022) 032003, 10.1103/PhysRevD.105.032003
26. U. A. Acharya et al., Transverse single-spin asymmetries of midrapidity π^0 and η mesons in polarized $p+p$ collisions at $\sqrt{s} = 200$ GeV, Phys. Rev. D 103 (2021) 052009, 10.1103/PhysRevD.103.052009
27. A. Adare et al., Measurement of transverse-single-spin asymmetries for midrapidity and forward-rapidity production of hadrons in polarized p+p collisions at $\sqrt{s}$ =200 and 62.4 GeV, Phys. Rev. D 90 (2014) 012006, 10.1103/PhysRevD.90.012006
28. U. D'Alesio, et al., Unraveling the Gluon Sivers Function in Hadronic Collisions at RHIC, Phys. Rev. D 99 (2019) 036013, 10.1103/PhysRevD.99.036013
29. H. Beppu, et al., Three-gluon contribution to the single spin asymmetry for light hadron production in pp collision, Phys. Rev. D 89 (2014) 034029, 10.1103/PhysRevD.89.034029
30. U. A. Acharya et al., Probing Gluon Spin-Momentum Correlations in Transversely Polarized Protons through Midrapidity Isolated Direct Photons in p↑+p Collisions at s=200 GeV, Phys. Rev. Lett. 127 (2021) 162001, 10.1103/PhysRevLett.127.162001

31. D. L. Adams et al., Measurement of single spin asymmetry for direct photon production in p p collisions at 200-GeV/c, Phys. Lett. B 345 (1995) 569, 10.1016/0370-2693(94)01695-9

32. H. Beppu, et al., Three-gluon contribution to the single spin asymmetry for light hadron production in pp collision, Phys. Rev. D 89 (2014) 034029, 10.1103/PhysRevD.89.034029

33. U. A. Acharya et al., Improving constraints on gluon spin-momentum correlations in transversely polarized protons via midrapidity open-heavy-flavor electrons in $p^{\uparrow} + p$ collisions at $\sqrt{s} = 200$ GeV (2022)

34. Z.-B. Kang, et al., Accessing tri-gluon correlations in the nucleon via the single spin asymmetry in open charm production, Phys. Rev. D 78 (2008) 114013, 10.1103/PhysRevD.78.114013

35. Y. Koike and S. Yoshida, Probing the three-gluon correlation functions by the single spin asymmetry in $p^{\uparrow}p \to DX$, Phys. Rev. D 84 (2011) 014026, 10.1103/PhysRevD.84.014026

36. C. Aidala et al., Cross section and transverse single-spin asymmetry of muons from open heavy-flavor decays in polarized p+p collisions at $\sqrt{s} = 200$ GeV, Phys. Rev. D 95 (2017) 112001, 10.1103/PhysRevD.95.112001

37. C. Aidala et al., Nuclear Dependence of the Transverse Single-Spin Asymmetry in the Production of Charged Hadrons at Forward Rapidity in Polarized $p + p$, p+Al, and p+Au Collisions at $\sqrt{s_{NN}} = 200$ GeV, Phys. Rev. Lett. 123 (2019) 122001, 10.1103/PhysRevLett.123.122001

38. Z.-B. Kang and F. Yuan, Single Spin Asymmetry Scaling in the Forward Rapidity Region at RHIC, Phys. Rev. D 84 (2011) 034019, 10.1103/PhysRevD.84.034019

39. S. Benić and Y. Hatta, Single spin asymmetry in forward pA collisions: Phenomenology at RHIC, Phys. Rev. D 99 (2019) 094012, 10.1103/PhysRevD.99.094012

40. U. A. Acharya et al., Transverse single spin asymmetries of forward neutrons in $p + p$, p+Al and p+Au collisions at $\sqrt{s_{NN}} = 200$ GeV as a function of transverse and longitudinal momenta, Phys. Rev. D 105 (2022) 032004, 10.1103/PhysRevD.105.032004

41. G. Mitsuka, (private communication), based on [42]

42. G. Mitsuka, Recently measured large A_N for forward neutrons in $p^{\uparrow}A$ collisions at $\sqrt{s_{NN}} = 200$ GeV explained through simulations of ultraperipheral collisions and hadronic interactions, Phys. Rev. C 95 (2017) 044908, 10.1103/PhysRevC.95.044908